ELSEVIER

Polymer 43 (2002) 4745–4761

polymer

www.elsevier.com/locate/polymer

# The effect of annealing on the time-dependent behavior of isotactic polypropylene at finite strains

Aleksey D. Drozdov*, Jesper deClaville Christiansen

*Department of Production, Aalborg University, Fibigerstraede 16, DK-9220 Aalborg, Denmark*

Received 11 February 2002; received in revised form 10 May 2002; accepted 10 May 2002

**Abstract**

Four series of tensile relaxation tests are performed on isotactic polypropylene at elongations up to the necking point. In the first series of experiments, injection-molded samples are used without thermal pre-treatment. In the other series, the specimens are annealed for 24 h prior to testing at 110, 120 and 130 °C, respectively. Results of mechanical experiments are compared with DSC measurements.

A constitutive model is derived for the time-dependent response of semicrystalline polymers at finite strains. A polymer is treated as an equivalent temporary network of macromolecules bridged by junctions (physical cross-links, entanglements and crystalline lamellae). At random times chains separate from their junctions and merge with new ones (the viscoelastic response), whereas junctions slip with respect to their positions in the bulk material (the viscoplastic behavior). The network is thought of as an ensemble of active meso-regions with various potential energies for detachment of chains from temporary nodes and passive meso-domains, where separation of chains is prevented by surrounding radial and tangential lamellae.

Experimental data demonstrate that the content of active meso-domains increases with elongation ratio driven by the release of constrained amorphous phase induced by fragmentation of lamellae. In the sub-critical region of deformation (relatively small strains), the growth of the concentration of active meso-regions is associated with breakage of subsidiary (thin) lamellae developed at annealing. In the post-critical region (large strains), an increase in the fraction of active amorphous domains is attributed to disintegration of primary (thick) lamellae. 

*Keywords:* Isotactic polypropylene; Annealing; Relaxation

## 1. Introduction

This paper is concerned with the effect of annealing on the viscoelastic behavior of isotactic polypropylene (iPP) at finite strains (up to the necking point). Isotactic polypropylene is chosen for the analysis because of numerous applications of this polymer in industry (oriented films for packaging, reinforcing fibers, non-woven fabrics, blends with thermoplastic elastomers, etc.).

The effect of annealing at elevated temperatures on the morphology of semicrystalline polymers has been a focus of attention during the past five years, see Refs. [1–11], to mention a few. The previous works concentrated on calorimetric and morphological analysis of transformations in the microstructure of crystallites. The influence of these transformations on the mechanical response of solid polymers was not studied in detail. The goal of this paper is to reveal some correlations between changes in the structure of crystalline lamellae at annealing (observed in DSC tests as the development of a low-temperature shoulder on melting curves) and alternation of relaxation curves measured in the sub-yield and post-yield regions of deformation.

The non-linear viscoelastic response of polypropylene was analyzed by Ward and Wolfe [12], see also Ward and Hadley [13], and Smart and Williams [14] three decades ago, and, more recently, by Wortmann and Schulz [15,16], Ariyama [17], Ariyama et al. [18], Dutta and Edward [19], Read and Tomlins [20], and Tomlins and Read [21].

Dynamic mechanical analysis shows two pronounced maxima on the plot of the loss tangent of iPP versus temperature [22,23]. The first maximum (β-transition in the interval between $T = -20$ and 10 °C) is associated with the glass transition in the most mobile part of the amorphous phase, whereas the other maximum (α-transition in the interval between $T = 70$ and 110 °C) is attributed to the glass transition in the remaining part of the amorphous

* Corresponding author. Tel.: +45-9815-8938; fax: +45-9815-3030.
*E-mail address:* drozdov@iprod.auc.dk (A.D. Drozdov).

0032-3861/01/$ - see front matter 
PII: S0032-3861(02)00315-4

phase (the so-called 'rigid amorphous fraction' [1]). This conclusion is confirmed by DSC traces for quenched PP that reveal an endoterm at $T = 70$ °C which may be ascribed to thermal activation of amorphous regions with restricted mobility at heating [23].

Isotactic polypropylene exhibits three different crystallographic forms: monoclinic α crystallites, (pseudo) hexagonal β structures, orthorhombic γ polymorphs, and 'smectic' mesophase [3]. At rapid cooling of the melt (which is typical of injection molding), α crystallites and smectic mesophase are mainly developed, whereas β and γ polymorphs arise as minority components [24]. A unique feature of α structures in iPP is the lamellar cross-hatching: development of transverse lamellae in spherulites that are oriented in the direction perpendicular to the direction of radial lamellae [7,8]. The characteristic size of α spherulites in injection-molded specimens is estimated as 100–200 μm [24,25]. These spherulites consist of crystalline lamellae with thickness of 10–20 nm [25]. The amorphous phase is located (i) between spherulites, (ii) inside spherulites between lamellar stacks ('liquid pockets' [1]), and (iii) between lamellae in lamellar stacks. It consists of (i) relatively mobile chains between spherulites, in liquid pockets and between radial lamellae inside lamellar stacks, and (ii) severely restricted chains in the regions bounded by radial and tangential lamellae.

Annealing of iPP at an elevated temperature results in (i) secondary crystallization of a part of the amorphous phase, (ii) thickening of radial lamellae, (iii) development of subsidiary lamellae, and (iv) growth of the crystal perfection [8]. Other morphological changes in iPP driven by thermal treatment are the subject of debate. Some researchers [11, 25,26] conclude that the fraction of β spherulites increases at annealing in the interval of temperatures between 110 and 130 °C, which enhances ductility of iPP and improves its impact properties. According to other authors [7,23], annealing of iPP induces transformation of smectic mesophase into α polymorph without noticeable development of β structures.

Mechanical loading results in inter-lamellar separation, rotation and twist of lamellae, fine and coarse slip of lamellar blocks and their fragmentation [23,27]. Stretching of iPP specimens causes chain slip through the crystals, sliding and breakage of tie chains [28,29], and activation of constrained amorphous regions driven by lamellar disintegration. In the post-yield region, these alternations of the microstructure result in cavitation, formation of fibrills and stress-induced crystallization [30].

Morphological transformations in iPP driven by thermomechanical factors cannot be adequately described by a constitutive model with a small number of adjustable parameters. To develop stress–strain relations, a method of 'homogenization of microstructure' [31] is applied. According to this approach, an equivalent phase is introduced whose deformation captures essential features of the response of a semicrystalline polymer with a complicated microstructure. An amorphous phase is chosen as the equivalent phase for the following reasons:

1. The viscoelastic response of semicrystalline polymers is conventionally associated with rearrangement of chains in amorphous regions [25].
2. Sliding of tie chains along and their detachment from lamellae play the key role in the time-dependent response of semicrystalline polymers [28,29].
3. The viscoplastic flow in semicrystalline polymers is assumed to be 'initiated in the amorphous phase before transitioning into the crystalline phase' [32].
4. Conventional models for polyethylene [31], polypropylene [33,34] and poly(ethylene terephthalate) [35] treat these polymers as networks of macromolecules.

Above the glass transition temperature for the mobile amorphous phase, iPP is thought of as a network of macromolecules bridged by junctions. Deformation of a specimen induces slip of junctions with respect to their positions in the bulk material. Sliding of junctions reflects slippage of tie molecules along lamellae and fine slip of lamellar blocks.

With reference to the concept of transient networks [36–38], the viscoelastic response of iPP is modeled as separation of active chains from their junctions and attachment of dangling chains to temporary nodes. Detachment of chains from junctions is treated as a thermally activated process whose rate is governed by the Eyring equation [39].

A network of macromolecules is thought of as an ensemble of meso-regions (MR) with various activation energies for separation of active strands. The heterogeneity of the network is attributed to (i) the influence of crystallites on rearrangement of surrounding chains and (ii) the local inhomogeneity of amorphous phase induced by density fluctuations. Two types of MRs are distinguished: (i) active domains, where strands separate from junctions as they are thermally agitated (mobile part of the amorphous phase), and (ii) passive domains, where detachment of chains from junctions is prevented by surrounding lamellae (rigid amorphous fraction). Stretching of a specimen results in the growth of the content of active MRs driven by release of the amorphous phase in passive meso-domains due to fragmentation of lamellae.

The objective of this study is three-fold:

1. To report experimental data in DSC tests and in tensile relaxation tests on specimens not subjected to thermal treatment and on samples annealed at various temperatures, $T$, in the interval between 110 and 130 °C.
2. To derive constitutive equations for the viscoelastic response of semicrystalline polymers at finite strains.
3. To assess the effect of annealing on the time-dependent behavior of iPP and to reveal some correlations between observations in calorimetric and mechanical tests.

The exposition is organized as follows. Section 2 deals with the kinetics of rearrangement of strands in active meso-domains. Kinematic equations for sliding of temporary junctions are developed in Section 3. Stress–strain relations are derived in Section 4 by using the laws of thermodynamics. The constitutive equations are simplified for uniaxial tension of a bar in Section 5. The specimens and the experimental procedure are described in Section 6. Adjustable parameters in the constitutive equations are found in Section 7 by fitting observations. A brief discussion of our findings is presented in Section 8. Some concluding remarks are formulated in Section 9.

## 2. Rearrangement of active strands

A semicrystalline polymer is treated as a temporary network of chains bridged by junctions. The network is modeled as an ensemble of meso-regions with various potential energies for detachment of strands from their junctions. Two types of meso-domains are distinguished: passive and active. In passive MRs, all nodes are thought of as permanent. In active MRs, active strands (whose ends are connected to contiguous nodes) separate from the temporary junctions at random times when they are thermally agitated. An active chain whose end detaches from a junction is transformed into a dangling chain. A dangling chain returns into the active state when its free end captures a nearby junction at a random instant.

Denote by $X_a$ the number of strands merged with the network in active MRs, and by $X_p$ the number of strands connected to the network in passive MRs. At stretching, some crystalline lamellae (restricting mobility of chains in passive MRs) break, which results in a growth of the number of strands to be rearranged. As a consequence, the number of strands in active MRs increases and the number of strands in passive meso-domains decreases. Under a time-dependent loading program, the quantities $X_a$ and $X_p$ are functions of time $t$ that obey the conservation law

$$X_a(t) + X_p(t) = X, \tag{1}$$

where $X$ is the average number of active strands per unit mass of a polymer (this quantity is assumed to be time-independent).

Rearrangement of strands in active MRs is thought of as a thermally activated process. The rate of detachment of active strands from their junctions in a MR with potential energy $\bar{\omega}$ is given by the Eyring equation [39]

$$\Gamma = \Gamma_a \exp\left(-\frac{\bar{\omega}}{k_B T}\right),$$

where $k_B$ is Boltzmann's constant, $T$ is the absolute temperature, and the pre-factor $\Gamma_a$ is independent of energy $\bar{\omega}$ and temperature $T$. Introducing the dimensionless activation energy $\omega = \bar{\omega}/(k_B T_0)$, where $T_0$ is a reference temperature, we arrive at the formula

$$\Gamma = \Gamma_a \exp(-\omega). \tag{2}$$

The distribution of active MRs with various potential energies is described by the probability density $p(\omega)$ that equals the ratio of the number, $N_a(t, \omega)$, of active meso-domains with energy $\omega$ at instant $t$ to the total number of active MRs

$$N_a(t, \omega) = X_a(t) p(\omega). \tag{3}$$

We suppose that the distribution function, $p(\omega)$, for potential energies of active MRs is not affected by mechanical factors.

An ensemble of active meso-domains is described by the function $n_a(t, \tau, \omega)$ that equals the number of active strands at time $t$ (per unit mass) belonging to active MRs with potential energy $\omega$ that have last been rearranged before instant $\tau \in [0, t]$. In particular, $n_a(0, 0, \omega)$ is the number (per unit mass) of active strands in active MRs with potential energy $\omega$ in a stress-free medium

$$n_a(0, 0, \omega) = N_a(0, \omega), \tag{4}$$

and $n_a(t, t, \omega)$ is the number (per unit mass) of active strands in active MRs with potential energy $\omega$ in the deformed state at time $t$ (the initial time $t = 0$ corresponds to the instant when external loads are applied)

$$n_a(t, t, \omega) = N_a(t, \omega). \tag{5}$$

The amount

$$\frac{\partial n_a}{\partial \tau}(t, \tau, \omega)\Big|_{t=\tau} d\tau$$

equals the number (per unit mass) of dangling strands in active MRs with potential energy $\omega$ that merge with the network within the interval $[\tau, \tau + d\tau]$, and the quantity

$$\frac{\partial n_a}{\partial \tau}(t, \tau, \omega)\, d\tau$$

is the number of these strands that have not detached from temporary junctions during the interval $[\tau, t]$. The number (per unit mass) of strands in active MRs that separate (for the first time) from the network within the interval $[t, t + dt]$ reads

$$-\frac{\partial n_a}{\partial t}(t, 0, \omega)\, dt.$$

The number (per unit mass) of strands in active MRs that merged with the network during the interval $[\tau, \tau + d\tau]$ and, afterwards, separated from the network within the interval $[t, t + dt]$ is given by

$$-\frac{\partial^2 n_a}{\partial t \partial \tau}(t, \tau, \omega)\, dt\, d\tau.$$

The rate of detachment, $\Gamma$, equals the ratio of the number of active strands that separate from the network per unit time to the current number of active strands. Applying this definition to active strands that merged with the network

during the interval $[\tau, \tau + d\tau]$ and separated from temporary junctions within the interval $[t, t + dt]$, we find that

$$\frac{\partial^2 n_a}{\partial t \partial \tau}(t, \tau, \omega) = -\Gamma(\omega) \frac{\partial n_a}{\partial \tau}(t, \tau, \omega). \quad (6)$$

Changes in the function $n_a(t, 0, \omega)$ are governed by two processes:

1. Detachment of active strands from temporary nodes.
2. Mechanically induced activation of passive MRs.

The kinetic equation for this function reads

$$\frac{\partial n_a}{\partial t}(t, 0, \omega) = -\Gamma(\omega) n_a(t, 0, \omega) + \frac{\partial N_a}{\partial t}(t, \omega). \quad (7)$$

The solution of Eq. (7) with initial condition (4) is given by

$$n_a(t, 0, \omega) = N_a(0, \omega) \exp[-\Gamma(\omega) t] + \int_0^t \frac{\partial N_a}{\partial t}(\tau, \omega) \exp[-\Gamma(\omega)(t - \tau)] \, d\tau. \quad (8)$$

Eq. (6) implies that

$$\frac{\partial n_a}{\partial \tau}(t, \tau, \omega) = \varphi(\tau, \omega) \exp[-\Gamma(\omega)(t - \tau)], \quad (9)$$

where

$$\varphi(\tau, \omega) = \frac{\partial n_a}{\partial \tau}(t, \tau, \omega)\Big|_{t=\tau}.$$

It follows from Eq. (5) that

$$n_a(t, 0, \omega) + \int_0^t \frac{\partial n_a}{\partial \tau}(t, \tau, \omega) \, d\tau = N_a(t, \omega). \quad (10)$$

Differentiation of Eq. (10) with respect to time yields

$$\varphi(t, \omega) + \frac{\partial n_a}{\partial t}(t, 0, \omega) + \int_0^t \frac{\partial^2 n_a}{\partial t \partial \tau}(t, \tau, \omega) \, d\tau = \frac{\partial N_a}{\partial t}(t, \omega).$$

This equality together with Eqs. (6), (7) and (10) results in

$$\varphi(t, \omega) = \Gamma(\omega) N_a(t, \omega).$$

Combining this expression with Eq. (9), we find that

$$\frac{\partial n_a}{\partial \tau}(t, \tau, \omega) = \Gamma(\omega) N_a(t, \omega) \exp[-\Gamma(\omega)(t - \tau)]. \quad (11)$$

Rearrangement of active strands in active MRs is described by Eqs. (2), (3), (8) and (11). These relations are determined by (i) the distribution function $p(\omega)$ for active MRs with various potential energies $\omega$, and (ii) the concentration of active MRs

$$\kappa_a(t) = \frac{X_a(t)}{X}. \quad (12)$$

Separation of active strands from their junctions and detachment of dangling chains to the network reflect the viscoelastic response of a semicrystalline polymer. The viscoplastic behavior is associated with mechanically induced sliding of junctions with respect to their reference positions in the bulk material.

## 3. Sliding of junctions

Denote by $\mathbf{r}_0$ the radius vector of an arbitrary point in the reference state and by $\mathbf{r}(t)$ its radius vector in the deformed state at time $t \geq 0$. Transition from the reference state to the actual state is determined by the deformation gradient

$$\mathbf{F}^0(t) = \frac{\partial \mathbf{r}(t)}{\partial \mathbf{r}_0}. \quad (13)$$

Sliding of junctions with respect to their reference positions is modeled as a transformation of the reference state, when a point with the initial radius vector $\mathbf{r}_0$ moves to the point with a radius vector $\mathbf{r}_s(t)$. This transition is described by the deformation gradient

$$\mathbf{F}_s(t) = \frac{\partial \mathbf{r}_s(t)}{\partial \mathbf{r}_0}.$$

Transformation of the new reference state into the deformed state is characterized by the deformation gradient

$$\mathbf{F}_e(t) = \frac{\partial \mathbf{r}(t)}{\partial \mathbf{r}_s(t)}.$$

The subscript indices 's' and 'e' indicate that the corresponding deformation gradients describe sliding of junctions and elastic deformation (in the sense that the strain energy of a strand is a function of $\mathbf{F}_e$), respectively.

To simplify the analysis, we suppose that the network is incompressible. This hypothesis is based on the assumptions that (i) the excluded-volume effect and other multi-chain effects are screened for an individual strand by surrounding macromolecules, and (ii) the energy of interaction between strands is accounted for with the help of the incompressibility condition [38].

According to the chain rule for differentiation, the tensors $\mathbf{F}^0(t)$, $\mathbf{F}_s(t)$ and $\mathbf{F}_e(t)$ are connected by the conventional relationship

$$\mathbf{F}^0(t) = \mathbf{F}_e(t) \cdot \mathbf{F}_s(t), \quad (14)$$

where the dot denotes inner product.

Differentiation of Eq. (13) with respect to time implies that

$$\frac{d\mathbf{F}^0}{dt}(t) = \frac{\partial \mathbf{v}(t)}{\partial \mathbf{r}_0} = \frac{\partial \mathbf{v}(t)}{\partial \mathbf{r}(t)} \cdot \frac{\partial \mathbf{r}(t)}{\partial \mathbf{r}_0},$$

where $\mathbf{v}(t)$ is the velocity vector. Introducing the velocity gradient

$$\mathbf{L}(t) = \frac{\partial \mathbf{v}(t)}{\partial \mathbf{r}(t)},$$

and using Eq. (13), we find that

$$\frac{d\mathbf{F}^0}{dt}(t) = \mathbf{L}(t)\cdot\mathbf{F}^0(t). \tag{15}$$

Bearing in mind that

$$\frac{d}{dt}[\mathbf{F}^0(t)]^{-1} = -[\mathbf{F}^0(t)]^{-1}\cdot\frac{d\mathbf{F}^0}{dt}(t)\cdot[\mathbf{F}^0(t)]^{-1},$$

we obtain

$$\frac{d}{dt}[\mathbf{F}^0(t)]^{-1} = -[\mathbf{F}^0(t)]^{-1}\cdot\mathbf{L}(t). \tag{16}$$

By analogy with Eqs. (15) and (16), we write

$$\frac{d\mathbf{F}_s}{dt}(t) = \mathbf{L}_s(t)\cdot\mathbf{F}_s(t), \qquad \frac{d\mathbf{F}_s^{-1}}{dt}(t) = -\mathbf{F}_s^{-1}(t)\cdot\mathbf{L}_s(t), \tag{17}$$

where $\mathbf{L}_s(t)$ is the velocity gradient for sliding of junctions. It follows from Eq. (14) that

$$\frac{d\mathbf{F}_e}{dt}(t) = \frac{d}{dt}\Big[\mathbf{F}^0(t)\cdot\mathbf{F}_s^{-1}(t)\Big] = \frac{d\mathbf{F}^0}{dt}(t)\cdot\mathbf{F}_s^{-1}(t) + \mathbf{F}^0(t)\cdot\frac{d\mathbf{F}_s^{-1}}{dt}(t).$$

Substitution of Eqs. (15) and (17) into this equality results in

$$\frac{d\mathbf{F}_e}{dt}(t) = \mathbf{L}(t)\cdot\mathbf{F}_e(t) - \mathbf{F}_e(t)\cdot\mathbf{L}_s(t). \tag{18}$$

The right and left Cauchy–Green tensors for elastic deformation are given by

$$\mathbf{C}_e^0(t) = \mathbf{F}_e^T(t)\cdot\mathbf{F}_e(t), \qquad \mathbf{B}_e^0(t) = \mathbf{F}_e(t)\cdot\mathbf{F}_e^T(t), \tag{19}$$

where T stands for transpose. We differentiate the first equality in Eq. (19) with respect to time, use Eq. (18), and find that

$$\frac{d\mathbf{C}_e^0}{dt}(t) = 2\mathbf{F}_e^T(t)\cdot\mathbf{D}(t)\cdot\mathbf{F}_e(t) - \mathbf{L}_s^T(t)\cdot\mathbf{C}_e^0(t) - \mathbf{C}_e^0(t)\cdot\mathbf{L}_s(t), \tag{20}$$

where

$$\mathbf{D}(t) = \frac{1}{2}[\mathbf{L}(t) + \mathbf{L}^T(t)]$$

is the rate-of-strain tensor. Taking into account that

$$\frac{d}{dt}\Big[\mathbf{C}_e^0(t)\Big]^{-1} = -\Big[\mathbf{C}_e^0(t)\Big]^{-1}\cdot\frac{d\mathbf{C}_e^0}{dt}(t)\cdot\Big[\mathbf{C}_e^0(t)\Big]^{-1},$$

and using Eq. (20), we arrive at the formula

$$\frac{d}{dt}\left[\mathbf{C}_e^0(t)\right]^{-1} = -2\left[\mathbf{F}_e^T(t)\right]^{-1}\cdot\mathbf{D}(t)\cdot\left[\mathbf{F}_e^T(t)\right]^{-1} + \left[\mathbf{C}_e^0(t)\right]^{-1}\cdot\mathbf{L}_s^T(t) + \mathbf{L}_s(t)\cdot\left[\mathbf{C}_e^0(t)\right]^{-1}. \tag{21}$$

The first principal invariant of the right Cauchy–Green tensor $\mathbf{C}_e^0(t)$ reads

$$I_1^0(t) = \mathbf{C}_e^0(t) : \mathbf{I},$$

where $\mathbf{I}$ is the unit tensor and the colon stands for convolution. It follows from this equality and Eq. (20) that

$$\frac{dI_1^0}{dt}(t) = 2\Big[\mathbf{F}_e(t)\cdot\mathbf{F}_e^T(t)\Big] : \mathbf{D}(t) - 2\mathbf{C}_e^0(t) : \mathbf{D}_s(t), \tag{22}$$

where

$$\mathbf{D}_s(t) = \frac{1}{2}\Big[\mathbf{L}_s(t) + \mathbf{L}_s^T(t)\Big]$$

is the rate-of-strain tensor for sliding of junctions. Eqs. (19) and (22) imply that

$$\frac{dI_1^0}{dt}(t) = 2\Big[\mathbf{B}_e^0(t) : \mathbf{D}(t) - \mathbf{C}_e^0(t) : \mathbf{D}_s(t)\Big]. \tag{23}$$

For an incompressible medium, the second principal invariant of the right Cauchy–Green tensor $\mathbf{C}_e^0(t)$ is given by

$$I_2^0(t) = \Big[\mathbf{C}_e^0(t)\Big]^{-1} : \mathbf{I}.$$

Combining this equality with Eqs. (19) and (21), we find that

$$\frac{dI_2^0}{dt}(t) = -2\Big\{\Big[\mathbf{B}_e^0(t)\Big]^{-1} : \mathbf{D}(t) - \Big[\mathbf{C}_e^0(t)\Big]^{-1} : \mathbf{D}_s(t)\Big\}. \tag{24}$$

It follows from Eqs. (23) and (24) that the derivative of an arbitrary smooth function $\phi$ of the first two principal invariants of the right Cauchy–Green tensor $\mathbf{C}_e^0(t)$ is determined by the formula

$$\frac{d\phi}{dt}\Big(I_1^0(t), I_2^0(t)\Big) = 2\Big\{\Big[\phi_{,1}^0(t)\mathbf{B}_e^0(t) - \phi_{,2}^0(t)\Big(\mathbf{B}_e^0(t)\Big)^{-1}\Big] : \mathbf{D}(t) - \Big[\phi_{,1}^0(t)\mathbf{C}_e^0(t) - \phi_{,2}^0(t)\Big(\mathbf{C}_e^0(t)\Big)^{-1}\Big] : \mathbf{D}_s(t)\Big\}, \tag{25}$$

where

$$\phi_{,k}^0(t) = \frac{\partial\phi}{\partial I_k^0}\Big(I_1^0(t), I_2^0(t)\Big) \qquad k = 1, 2.$$

Eq. (20) describes evolution of the right Cauchy–Green tensor $\mathbf{C}_e^0(t)$ for strands that were bridged to their junctions in the stress-free state and have not detached from these junctions within the interval $[0, t]$. For a strand that merged with the network at some instant $\tau \in [0, t]$ and has remained linked to the network during the interval $[\tau, t]$, transformation of the deformed state at time $\tau$ into the deformed state at time $t$ is characterized by the deformation gradient

$$\mathbf{F}(t, \tau) = \mathbf{F}^0(t)\cdot[\mathbf{F}^0(\tau)]^{-1}.$$

Transformation of the reference state into the deformed state is described by the deformation gradient

$$\mathbf{F}_s(t, \tau) = \mathbf{F}_s(t)\cdot\mathbf{F}_s^{-1}(\tau).$$

The elastic deformation gradient $\mathbf{F}_e(t,\tau)$ is expressed in terms of the deformation gradients $\mathbf{F}(t,\tau)$ and $\mathbf{F}_s(t,\tau)$ by means of Eq. (14), which implies that

$$\mathbf{F}_e(t,\tau)=\mathbf{F}^0(t)\cdot\Big[\mathbf{F}^0(\tau)\Big]^{-1}\cdot\mathbf{F}_s(\tau)\cdot\mathbf{F}_s^{-1}(t). \tag{26}$$

The right and left Cauchy–Green tensors, $\mathbf{C}_e(t,\tau)$ and $\mathbf{B}_e(t,\tau)$, are given by Eq. (19). Combining these equalities with Eq. (26), we obtain

$$\mathbf{C}_e(t,\tau)=\mathbf{F}_s^{-T}(t)\cdot\mathbf{F}_s^{T}(\tau)\cdot\Big[\mathbf{F}^0(\tau)\Big]^{-T}\cdot\mathbf{C}^0(t)\cdot\Big[\mathbf{F}^0(\tau)\Big]^{-1}\cdot\mathbf{F}_s(\tau)\cdot\mathbf{F}_s^{-1}(t), \tag{27}$$

$$\mathbf{B}_e(t,\tau)=\mathbf{F}^0(t)\cdot\Big[\mathbf{F}^0(\tau)\Big]^{-1}\cdot\mathbf{F}_s(\tau)\cdot\mathbf{C}_s^{-1}(t)\cdot\mathbf{F}_s^{T}(\tau)\cdot\Big[\mathbf{F}^0(\tau)\Big]^{-T}\cdot[\mathbf{F}^0(t)]^{T},$$

where

$$\mathbf{C}^0(t)=\Big[\mathbf{F}^0(t)\Big]^{T}\cdot\mathbf{F}^0(t),\qquad \mathbf{C}_s(t)=\mathbf{F}_s^{T}(t)\cdot\mathbf{F}_s(t). \tag{28}$$

It follows from Eqs. (15) and (28) that

$$\frac{d\mathbf{C}^0}{dt}(t)=2\Big[\mathbf{F}^0(t)\Big]^{T}\cdot\mathbf{D}(t)\cdot\mathbf{F}^0(t). \tag{29}$$

Differentiating the first equality in Eq. (27) with respect to $t$ and using Eqs. (17) and (29), we find that

$$\frac{\partial\mathbf{C}_e}{\partial t}(t,\tau)=-\mathbf{L}_s^{T}(t)\cdot\mathbf{C}_e(t,\tau)-\mathbf{C}_e(t,\tau)\cdot\mathbf{L}_s(t)+2\mathbf{F}_s^{-T}(t)\cdot\mathbf{F}_s^{T}(\tau)\cdot\Big[\mathbf{F}^0(\tau)\Big]^{-T}\cdot\times\Big[\mathbf{F}^0(t)\Big]^{T}\cdot\mathbf{D}(t)\cdot\mathbf{F}^0(t)\cdot\Big[\mathbf{F}^0(\tau)\Big]^{-1}\cdot\mathbf{F}_s(\tau)\cdot\mathbf{F}_s^{-1}(t). \tag{30}$$

Eqs. (27) and (30) together with the formula

$$\frac{\partial\mathbf{C}_e^{-1}}{\partial t}(t,\tau)=-\mathbf{C}_e^{-1}(t,\tau)\cdot\frac{\partial\mathbf{C}_e}{\partial t}(t,\tau)\cdot\mathbf{C}_e^{-1}(t,\tau)$$

imply that

$$\frac{\partial\mathbf{C}_e^{-1}}{\partial t}(t,\tau)=\mathbf{C}_e^{-1}(t,\tau)\cdot\mathbf{L}_s^{T}(t)+\mathbf{L}_s(t)\cdot\mathbf{C}_e(t,\tau)-2\mathbf{F}_s(t)\cdot\mathbf{F}_s^{-1}(\tau)\cdot\mathbf{F}^0(\tau)\cdot\Big[\mathbf{F}^0(t)\Big]^{-1}\cdot\mathbf{D}(t)\cdot\Big[\mathbf{F}^0(t)\Big]^{-T}\cdot\Big[\mathbf{F}^0(\tau)\Big]^{T}\cdot\mathbf{F}_s^{-T}(\tau)\cdot\mathbf{F}_s^{T}(t). \tag{31}$$

The first principal invariant of the Cauchy–Green tensor $\mathbf{C}_e(t,\tau)$ reads

$$I_1(t,\tau)=\mathbf{C}_e(t,\tau):\mathbf{I}.$$

Differentiating this equality with respect to $t$ and using Eqs. (27) and (30), we arrive at the formula

$$\frac{\partial I_1}{\partial t}(t,\tau)=2\big[\mathbf{B}_e(t,\tau):\mathbf{D}(t)-\mathbf{C}_e(t,\tau):\mathbf{D}_s(t)\big]. \tag{32}$$

The second principal invariant of the Cauchy–Green tensor $\mathbf{C}_e(t,\tau)$ is given by

$$I_2(t,\tau)=\mathbf{C}_e^{-1}(t,\tau):\mathbf{I}.$$

It follows from this equality and Eqs. (27) and (31) that

$$\frac{\partial I_2}{\partial t}(t,\tau)=-2\Big[\mathbf{B}_e^{-1}(t,\tau):\mathbf{D}(t)-\mathbf{C}_e^{-1}(t,\tau):\mathbf{D}_s(t)\Big]. \tag{33}$$

According to Eqs. (32) and (33), for an arbitrary smooth function $\phi$ of the first two principal invariants of the right Cauchy–Green tensor $\mathbf{C}_e(t,\tau)$

$$\frac{\partial\phi}{\partial t}(I_1(t,\tau),I_2(t,\tau))=2\Big\{\Big[\phi_{,1}(t,\tau)\mathbf{B}_e(t,\tau)-\phi_{,2}(t,\tau)\mathbf{B}_e^{-1}(t,\tau)\Big]:\mathbf{D}(t)-\Big[\phi_{,1}(t,\tau)\mathbf{C}_e(t,\tau)-\phi_{,2}(t,\tau)\mathbf{C}_e^{-1}(t,\tau)\Big]:\mathbf{D}_s(t)\Big\} \tag{34}$$

with

$$\phi_{,k}(t,\tau)=\frac{\partial\phi}{\partial I_k}(I_1(t,\tau),I_2(t,\tau))\qquad k=1,2.$$

Formulas (25) and (34) are employed to develop stress–strain relations for a semicrystalline polymer.

## 4. Constitutive equations

This study is confined to active loading processes, when stretching a specimen results in mechanically induced activation of passive meso-regions. The strain energy of an active strand bridged to the network in a stress-free state, $\bar{w}$, depends on the first two principal invariants $I_k^0(t)$ $(k=1,2)$ of the right Cauchy–Green tensor, $\mathbf{C}_e^0(t)$, for transition from the reference state to the deformed state at time $t$

$$\bar{w}(t,0)=w(I_1^0(t),I_2^0(t)).$$

The strain energy, $\bar{w}(t,\tau)$, of an active strand that has last been reformed at time $\tau\in[0,t]$ is a function of the first two principal invariants, $I_k(t,\tau)$, of the right Cauchy–Green tensor $\mathbf{C}_e(t,\tau)$

$$\bar{w}(t,\tau)=w(I_1(t,\tau),I_2(t,\tau)).$$

The same function, $w$, is employed to describe strain energies of strands in various meso-domains. This function is assumed to vanish in the reference state

$$w(I_1,I_2)|_{I_1=3,I_2=3}=0. \tag{35}$$

We do not dwell on an explicit expression for the function $w$. A survey of strain energy densities of rubber-like materials can be found in Ref. [40].

Summing the strain energies of active strands in passive meso-domains and those of active strands in active meso-regions (that merged with the network at various times $\tau\in[0,t]$) and neglecting the energy of interaction between

strands (which is taken into account by means of the incompressibility condition), we arrive at the mechanical energy per unit mass of a polymer

$$W(t)=\left[X_{\rm p}(t)+\int_0^\infty n(t,0,\omega)\,{\rm d}\omega\right]w\Big(I_1^0(t),I_2^0(t)\Big)+\int_0^t\left[\int_0^\infty\frac{\partial n}{\partial\tau}(t,\tau,\omega)\,{\rm d}\omega\right]w(I_1(t,\tau),I_2(t,\tau))\,{\rm d}\tau.$$

Differentiating this equality with respect to time and using Eqs. (25), (34) and (35), we obtain

$$\frac{{\rm d}W}{{\rm d}t}(t)=2\mathbf{A}(t):\mathbf{D}(t)-2\mathbf{A}_{\rm s}(t):\mathbf{D}_{\rm s}(t)-Y(t),\tag{36}$$

where

$$\mathbf{A}(t)=\left[X_{\rm p}(t)+\int_0^\infty n(t,0,\omega)\,{\rm d}\omega\right]\left[w_{,1}^0(t)\mathbf{B}_{\rm e}^0(t)-w_{,2}^0(t)\Big(\mathbf{B}_{\rm e}^0(t)\Big)^{-1}\right]+\int_0^t\left[\int_0^\infty\frac{\partial n}{\partial\tau}(t,\tau,\omega)\,{\rm d}\omega\right]\times\Big[w_{,1}(t,\tau)\mathbf{B}_{\rm e}(t,\tau)-w_{,2}(t,\tau)\mathbf{B}_{\rm e}^{-1}(t,\tau)\Big]{\rm d}\tau,\tag{37}$$

$$\mathbf{A}_{\rm s}(t)=\left[X_{\rm p}(t)+\int_0^\infty n(t,0,\omega)\,{\rm d}\omega\right]\left[w_{,1}^0(t)\mathbf{C}_{\rm e}^0(t)-w_{,2}^0(t)\Big(\mathbf{C}_{\rm e}^0(t)\Big)^{-1}\right]+\int_0^t\left[\int_0^\infty\frac{\partial n}{\partial\tau}(t,\tau,\omega)\,{\rm d}\omega\right]\times\Big[w_{,1}(t,\tau)\mathbf{C}_{\rm e}(t,\tau)-w_{,2}(t,\tau)\mathbf{C}_{\rm e}^{-1}(t,\tau)\Big]{\rm d}\tau,$$

$$Y(t)=-\left[\frac{{\rm d}X_{\rm p}}{{\rm d}t}(t)+\int_0^\infty\frac{\partial n}{\partial t}(t,0,\omega)\,{\rm d}\omega\right]w\Big(I_1^0(t),I_2^0(t)\Big)-\int_0^t\left[\int_0^\infty\frac{\partial^2 n}{\partial t\partial\tau}(t,\tau,\omega)\,{\rm d}\omega\right]w(I_1(t,\tau),I_2(t,\tau))\,{\rm d}\tau.$$

Taking into account that the first invariant of the tensor $\mathbf{D}_{\rm s}$ vanishes for isochoric deformations, we present Eq. (36) as follows

$$\frac{{\rm d}W}{{\rm d}t}(t)=2\mathbf{A}(t):\mathbf{D}(t)-2\mathbf{A}_{\rm s}'(t):\mathbf{D}_{\rm s}(t)-Y(t),\tag{38}$$

where the prime stands for the deviatoric component of a tensor.

For isothermal deformation of an incompressible medium, the Clausius–Duhem inequality reads

$$Q=-\frac{{\rm d}W}{{\rm d}t}+\frac{1}{\rho}\boldsymbol{\Sigma}':\mathbf{D}\ge 0,$$

where $\rho$ is mass density, $\boldsymbol{\Sigma}$ is the Cauchy stress tensor, and $Q$ is the internal dissipation per unit mass. Substitution of Eq. (38) into this equality results in

$$Q=\frac{1}{\rho}(\boldsymbol{\Sigma}'-2\rho\mathbf{A}):\mathbf{D}+2\mathbf{A}_{\rm s}^{'}:\mathbf{D}_{\rm s}+Y\ge 0.\tag{39}$$

It follows from Eqs. (1), (3), (6), (7) and (37) that

$$Y(t)=\int_0^\infty\Gamma(\omega)\left[n(t,0,\omega)w\Big(I_1^0(t),I_2^0(t)\Big)+\int_0^t\frac{\partial n}{\partial\tau}(t,\tau,\omega)w(I_1(t,\tau),I_2(t,\tau))\,{\rm d}\tau\right]{\rm d}\omega.$$

Because the functions $\Gamma(\omega)$, $w(I_1,I_2)$, $n(t,0,\omega)$ and $\partial n/\partial\tau(t,\tau,\omega)$ are non-negative, we find that the function $Y(t)$ is non-negative as well. This means that the dissipation inequality (39) is satisfied for an arbitrary deformation program, provided that (i) the expression in brackets vanishes and (ii) the rate-of-strain tensor for sliding of junctions $\mathbf{D}_{\rm s}$ is proportional to the tensor $\mathbf{A}_{\rm s}'$. The first condition results in the constitutive equation

$$\boldsymbol{\Sigma}(t)=-P(t)\mathbf{I}+2\rho\left\{\left[X_{\rm p}(t)+\int_0^\infty n(t,0,\omega)\,{\rm d}\omega\right]\left[w_{,1}^0(t)\mathbf{B}_{\rm e}^0(t)-w_{,2}^0(t)\Big(\mathbf{B}_{\rm e}^0(t)\Big)^{-1}\right]+\int_0^t\left[\int_0^\infty\frac{\partial n}{\partial\tau}(t,\tau,\omega)\,{\rm d}\omega\right]\times\Big[w_{,1}(t,\tau)\mathbf{B}_{\rm e}(t,\tau)-w_{,2}(t,\tau)\mathbf{B}_{\rm e}^{-1}(t,\tau)\Big]{\rm d}\tau\right\},\tag{40}$$

where $P$ is pressure. The other condition leads to the kinetic equation for sliding of junctions

$$\mathbf{D}_{\rm e}(t)=\alpha(t)[\mathbf{D}(t):\mathbf{D}(t)]^{1/2}\left\{\left[X_{\rm p}(t)+\int_0^\infty n(t,0,\omega)\,{\rm d}\omega\right]\times\left[w_{,1}^0(t)\mathbf{C}_{\rm e}^0(t)-w_{,2}^0(t)\Big(\mathbf{C}_{\rm e}^0(t)\Big)^{-1}\right]+\int_0^t\left[\int_0^\infty\frac{\partial n}{\partial\tau}(t,\tau,\omega)\,{\rm d}\omega\right]\times\Big[w_{,1}(t,\tau)\mathbf{C}_{\rm e}(t,\tau)-w_{,2}(t,\tau)\mathbf{C}_{\rm e}^{-1}(t,\tau)\Big]{\rm d}\tau\right\}^{'},\tag{41}$$

where $\alpha$ is a non-negative function of the Cauchy stress tensor $\boldsymbol{\Sigma}$ and the rate-of-strain tensors $\mathbf{D}$ and $\mathbf{D}_{\rm s}$ that obeys conventional axioms in continuum mechanics. The prefactor $[\mathbf{D}(t):\mathbf{D}(t)]^{1/2}$ in Eq. (41) ensures that the rate of sliding of junctions with respect to their reference positions is proportional to the strain rate. This assertion allows the viscoelastic and viscoplastic deformations to be distinguished: the behavior of a semicrystalline polymer in tests with time-independent deformations (relaxation) is entirely ascribed to rearrangement of active strands, whereas the

rate-dependent response at high-speed loadings is attributed to sliding of junctions.

Eq. (41) differs from conventional relations in finite elastoplasticity, where the rate of plastic flow is assumed to be proportional to the deviatoric part of the Cauchy stress tensor $\mathbf{\Sigma}$. Eqs. (40) and (41) demonstrate that for an arbitrary three-dimensional deformation, the tensor $\mathbf{D}_s$ is not proportional to $\mathbf{\Sigma}'$, except for the special cases when the right and left Cauchy–Green tensors coincide.

Our aim now is to simplify the constitutive Eqs. (40) and (41) for uniaxial extension of a specimen.

## 5. Uniaxial tension of a bar

Points of a bar refer to Cartesian coordinates $\{X_i\}$ $(i = 1,2,3)$ in the stress-free state, to Cartesian coordinates $\{x_i\}$ in the deformed state, and to Cartesian coordinates $\{\xi_i\}$ in the reference state at time $t$. Uniaxial tension of an incompressible medium is described by the formulas

$$x_1 = k(t)X_1, \qquad x_2 = k^{-1/2}(t)X_2, \qquad x_3 = k^{-1/2}(t)X_3, \tag{42}$$

where $k = k(t)$ is the extension ratio. It is assumed that transformation of the reference state is determined by the equations similar to Eq. (42)

$$\xi_1 = k_s(t)X_1, \qquad \xi_2 = k_s^{-1/2}(t)X_2, \qquad \xi_3 = k_s^{-1/2}(t)X_3,$$

where $k_s(t)$ is a function to be found. Omitting simple algebra, we find from Eq. (40) and the boundary condition of the stress-free lateral surface of the bar that the true longitudinal stress $\sigma$ is given by

$$\sigma(t) = 2\rho\Bigg\{\Bigg[X_p(t) + \int_0^\infty n(t,0,\omega)\,d\omega\Bigg]$$
$$\times\Bigg[w_{,1}^0(t) + w_{,2}^0(t)\frac{k_s(t)}{k(t)}\Bigg]\Bigg[\Bigg(\frac{k(t)}{k_s(t)}\Bigg)^2 - \frac{k_s(t)}{k(t)}\Bigg]$$
$$+ \int_0^t\Bigg[\int_0^\infty \frac{\partial n}{\partial \tau}(t,\tau,\omega)\,d\omega\Bigg]\Bigg[w_{,1}(t,\tau) + w_{,2}(t,\tau)\frac{k_s(t)k(\tau)}{k(t)k_s(\tau)}\Bigg]$$
$$\times\Bigg[\Bigg(\frac{k(t)k_s(\tau)}{k_s(t)k(\tau)}\Bigg)^2 - \frac{k_s(t)k(\tau)}{k(t)k_s(\tau)}\Bigg]d\tau\Bigg\}. \tag{43}$$

Eq. (41) implies the differential equation for the function $k_s$

$$\frac{dk_s}{dt}(t) = \alpha_1(t)\sigma(t)\frac{k_s(t)}{k(t)}\left|\frac{dk}{dt}(t)\right|, \qquad k_s(0) = 1, \tag{44}$$

where $\alpha_1 = \alpha/(2\rho)$.

To compare results of numerical simulation with the experimental data, we concentrate on a tensile relaxation test with

$$k(t) = \begin{cases} 1, & t < 0, \\ \lambda, & t \geq 0, \end{cases} \tag{45}$$

where $\lambda > 1$ is a constant. It follows from Eqs. (44) and (45) that $k_s(t) = \lambda_s$ for any $t > 0$. For the deformation program (45), the fractions of active, $X_a$, and passive, $X_p$, MRs become functions of the elongation ratio $\lambda$. The strain energy density per strand, $w$, depends on $\lambda$ and $\lambda_s$. Substitution of expressions (2), (3), (8), (12) and (45) into Eq. (43) results in the following expression for the engineering stress $\sigma_e = \sigma/\lambda$ :

$$\sigma_e(t,\lambda) = \sigma_0(\lambda)\Bigg\{1 - \kappa_a(\lambda)\int_0^\infty [1 - \exp(-\Gamma_a\exp(-\omega)t)]p(\omega)\,d\omega\Bigg\}, \tag{46}$$

where

$$\sigma_0(\lambda) = 2\rho X\lambda_s\Bigg[w_{,1}^0(\lambda,\lambda_s) + w_{,2}^0(\lambda,\lambda_s)\frac{\lambda_s}{\lambda}\Bigg]\Bigg[\frac{\lambda}{\lambda_s} - \Bigg(\frac{\lambda_s}{\lambda}\Bigg)^2\Bigg].$$

To fit experimental data, we adopt the random energy model [41] for the distribution of active MRs with various activation energies

$$p(\omega) = p_0\exp\Bigg[-\frac{(\omega - \bar{\Omega})^2}{2\Sigma^2}\Bigg] \quad (\omega \geq 0),$$
$$p(\omega) = 0 \quad (\omega < 0), \tag{47}$$

where $\bar{\Omega}$ and $\Sigma$ are adjustable parameters of the quasi-Gaussian probability density, and the constant $p_0$ is determined by the condition

$$\int_0^\infty p(\omega)\,d\omega = 1. \tag{48}$$

Setting $\omega_a = \ln\Gamma_a$ and introducing the notation $z = \omega - \omega_a$, we find from Eqs. (46) and (47) that

$$\sigma_e(t,\lambda) = \sigma_0(\lambda)\Bigg\{1 - p_0\kappa_a(\lambda)\int_{-\omega_a}^\infty \times[1 - \exp(-\exp(-z)t)]\exp\Bigg[-\frac{(z-\Omega)^2}{2\Sigma^2}\Bigg]dz\Bigg\},$$

where $\Omega = \bar{\Omega} - \omega_a$. Assuming the quasi-Gaussian distribution to be rather narrow (this condition will be verified by matching experimental data), we replace the lower limit of

integration by zero and arrive at the formula

$$\sigma_e(t,\lambda) = \sigma_0(\lambda)\Big\{1 - p_0\kappa_a(\lambda)\int_0^\infty \times[1-\exp(-\exp(-z)t)]\exp\Big[-\frac{(z-\Omega)^2}{2\Sigma^2}\Big]dz\Big\}. \quad (49)$$

Given an elongation ratio, $\lambda$, Eq. (49) is determined by four material constants:

1. The apparent average potential energy for separation of strands from temporary junctions $\Omega$.
2. The apparent standard deviation of potential energies for detachment of strands in active meso-regions $\Sigma$.
3. The concentration of strands in active meso-domains $\kappa_a$.
4. The engineering stress at the beginning of a relaxation test $\sigma_0$.

The quantities $\Omega$ and $\Sigma$ are assumed to be strain-independent, which implies that an individual relaxation curve is characterized by two adjustable parameters, $\kappa_a$ and $\sigma_0$. These amounts are found by fitting experimental data in tensile relaxation tests on iPP at various elongation ratios.

## 6. Experimental procedure

Isotactic polypropylene (Novolen 1100L) was supplied by BASF (Targor). ASTM dumbbell specimens were injection molded with length 148 mm, width 10 mm and thickness 3.8 mm. Four series of tests were performed. In the first series, the samples were used as produced without thermal pre-treatment. In the other series of tests, the specimens were annealed in an oven at the temperatures 110, 120 and 130 °C for 24 h and slowly cooled by air.

Differential scanning calorimetry measurements were carried out on STA 449/Netzsch apparatus at the heating rate 5 K/min. The specimens with mass of about 15 mg were tested in $Al_2O_2$ pans covered by lid in argon atmosphere. The thermal analyzer was calibrated with seven references ranging from In to Ni. The specific enthalpy of melting, $\Delta H_m$, equals 86.9 J/g for non-annealed specimens (the melting peak $T_m = 169$ °C) and 90.7, 99.9, 102.1 J/g for samples annealed at 110, 120 and 130 °C, respectively. The melting peak and the enthalpy of fusion for specimens not subjected to annealing are in fair agreement with observations by Collar et al. [42] ($T_m = 165$ °C, $\Delta H_m = 78.1$ J/g).

With reference to Wunderlich [43], we accept the value 209 J/g as the enthalpy of fusion for a fully crystalline polypropylene. The degree of crystallinity, $\kappa_c$, is estimated as 41.6% for samples not subjected to thermal treatment and 43.4, 47.8, 48.9% for annealed specimens, which implies

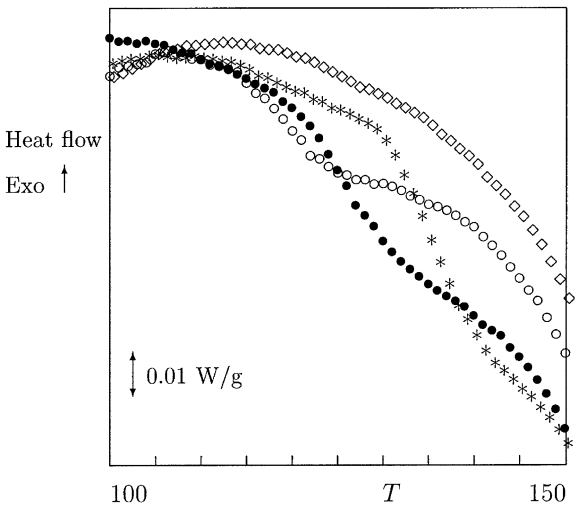


Fig. 1. DSC melting curves for isotactic polypropylene annealed at a temperature $T$. Symbols: experimental data. Diamonds: non-annealed samples; unfilled circles: $T = 110$ °C; filled circles: $T = 120$ °C; asterisks: $T = 130$ °C.

that $\kappa_c$ increases rather weakly, but consistently with annealing temperature $T$.

The shape of DSC curves is noticeably altered in the interval of temperatures between 100 and 150 °C. The DSC traces depicted in Fig. 1 are similar to those previously measured on iPP [3,4,7,8,11].

Uniaxial tensile relaxation tests were performed at room temperature on a testing machine Instron-5568 equipped with electro-mechanical sensors for the control of longitudinal strains in the active zone of samples (the distance between clips was about 50 mm). The tensile force was measured by a standard bad cell. The engineering stress $\sigma_e$ was determined as the ratio of the axial force to the cross-sectional area of the specimens in the stress-free state.

Mechanical tests were carried out at least one day after annealing of specimens to minimize the effect of physical aging on the time-dependent response. The specimens were loaded with a cross-head speed of 5 mm/min (that corresponded to the Hencky strain rate $\dot{\epsilon}_H = 1.1\times10^{-3}$ s$^{-1}$). The engineering stress–engineering strain diagrams ($\epsilon = k - 1$) are depicted in Fig. 2. These curves are similar in shape to the tensile stress–strain curves reported in Refs. [11,30].

The same data are re-plotted in Fig. 3 as the true longitudinal stress versus the elongation ratio $k$. This figure demonstrates that the apparent yield point (defined as the point where a transient growth of stress is transformed into a steady plastic flow) is not affected by annealing. The apparent necking point (determined as the point where the true stress starts to decrease with strain) is independent of the annealing temperature, $T$, but the elongation ratio for necking, $k_n$, for annealed specimens substantially exceeds that for samples not subjected to thermal treatment. It is worth noting that the apparent yield strains in Fig. 3 are

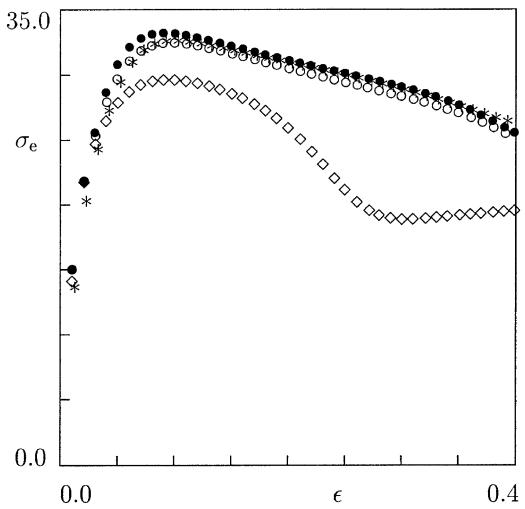


Fig. 2. The engineering stress $\sigma_e$ (MPa) versus strain $\epsilon$ in tensile tests with a constant cross-head speed. Symbols: experimental data on specimens annealed at a temperature $T$. Diamonds: non-annealed samples; unfilled circles: $T = 110$ °C; filled circles: $T = 120$ °C; asterisks: $T = 130$ °C.

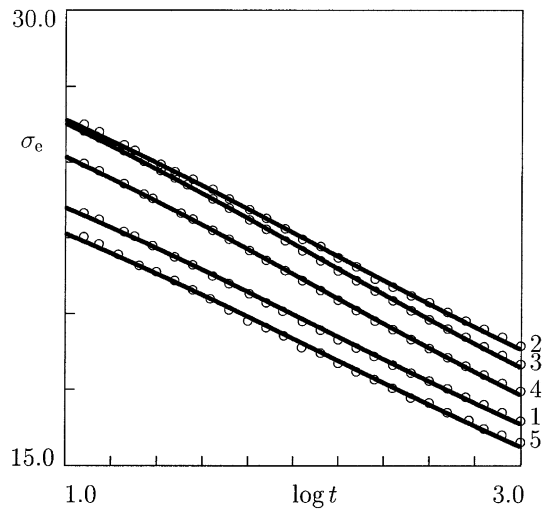


Fig. 4. The engineering stress $\sigma_e$ (MPa) versus time $t$ (s) in tensile relaxation tests on non-annealed specimens. Circles: experimental data. Solid lines: results of numerical simulation. Curve 1: $\epsilon = 0.04$; curve 2: $\epsilon = 0.08$; curve 3: $\epsilon = 0.12$; curve 4: $\epsilon = 0.16$; curve 5: $\epsilon = 0.20$.

noticeably larger than the yield strains determined as points of maxima on the engineering stress–engineering strain diagrams depicted in Fig. 2.

The series of relaxation experiments on non-annealed specimens contained five relaxation tests at the longitudinal strains $\epsilon_1 = 0.04$, $\epsilon_2 = 0.08$, $\epsilon_3 = 0.12$, $\epsilon_4 = 0.16$, and $\epsilon_5 = 0.20$. These strains correspond to the sub-yield and post-yield regions in Fig. 2.

Each relaxation test was performed on a new sample. No necking of specimens was observed (except for the test with $\epsilon_5 = 0.20$, where a weak neck was created at loading that remained stable within the relaxation period). In the $m$th relaxation test ($m = 1, \ldots, 5$), a specimen was loaded with the cross-head speed 5 mm/min up to the longitudinal strain $\epsilon_m$ that was preserved constant during the relaxation time $t_r = 20$ min.

The engineering stress, $\sigma_e$, is plotted versus the logarithm ($\log = \log_{10}$) of time $t$ (the instant $t = 0$ corresponds to the beginning of stress relaxation) in Fig. 4. This figure demonstrates that the slopes of relaxation curves monotonically increase with strain in the sub-yield region and slowly decrease with $\epsilon$ in the post-yield domain.

All series of relaxation experiments on annealed

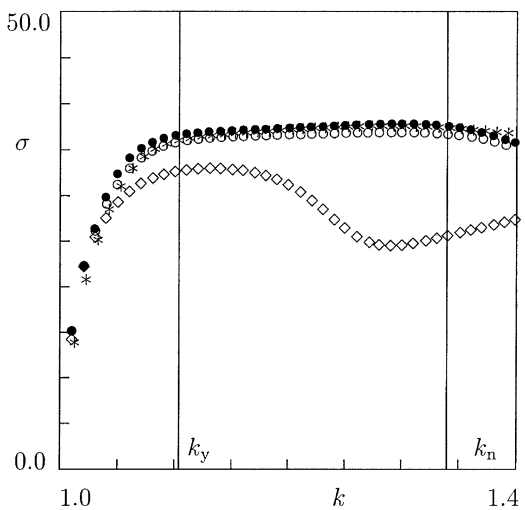


Fig. 3. The true stress $\sigma$ (MPa) versus the elongation ratio $k$ in tensile tests with a constant cross-head speed. Symbols: experimental data for specimens annealed at a temperature $T$. Diamonds: non-annealed samples; unfilled circles: $T = 110$ °C; filled circles: $T = 120$ °C; asterisks: $T = 130$ °C. Vertical lines indicate apparent elongation ratios for yielding, $k_y$, and necking, $k_n$, of annealed samples.

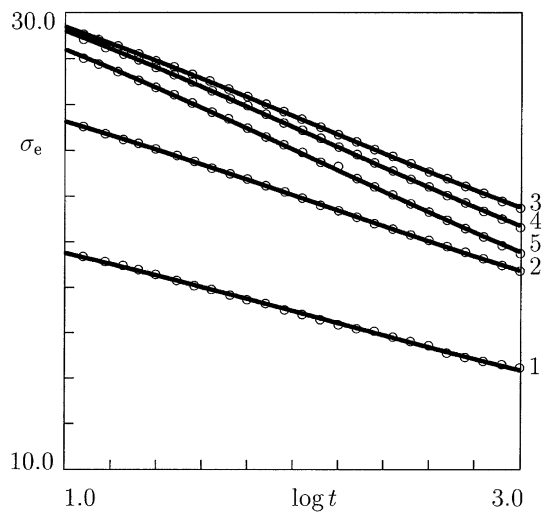


Fig. 5. The engineering stress $\sigma_e$ (MPa) versus time $t$ (s) in tensile relaxation tests on specimens annealed at $T = 110$ °C. Circles: experimental data. Solid lines: results of numerical simulation. Curve 1: $\epsilon = 0.02$; curve 2: $\epsilon = 0.04$; curve 3: $\epsilon = 0.08$; curve 4: $\epsilon = 0.12$; curve 5: $\epsilon = 0.16$.

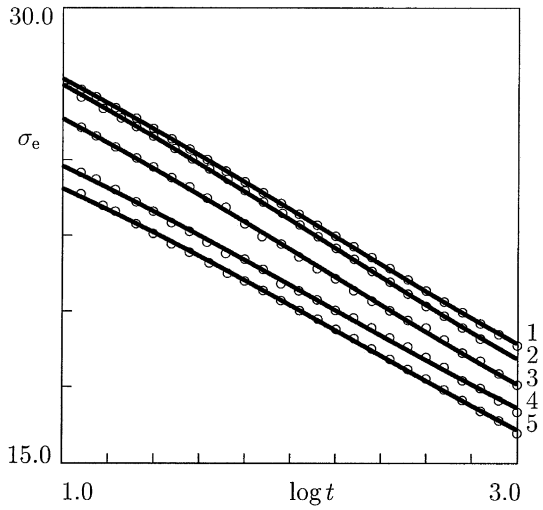


Fig. 6. The engineering stress $\sigma_e$ (MPa) versus time $t$ (s) in tensile relaxation tests on specimens annealed at $T = 110\,^{\circ}C$. Circles: experimental data. Solid lines: results of numerical simulation. Curve 1: $\epsilon = 0.18$; curve 2: $\epsilon = 0.20$; curve 3: $\epsilon = 0.24$; curve 4: $\epsilon = 0.28$; curve 5: $\epsilon = 0.32$.

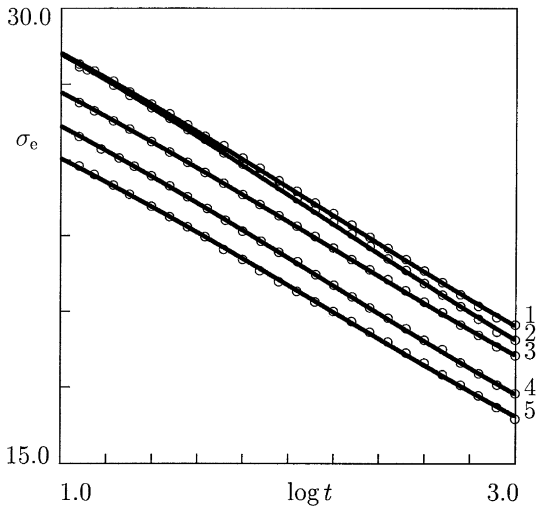


Fig. 8. The engineering stress $\sigma_e$ (MPa) versus time $t$ (s) in tensile relaxation tests on specimens annealed at $T = 120\,^{\circ}C$. Circles: experimental data. Solid lines: results of numerical simulation. Curve 1: $\epsilon = 0.18$; curve 2: $\epsilon = 0.20$; curve 3: $\epsilon = 0.24$; curve 4: $\epsilon = 0.28$; curve 5: $\epsilon = 0.32$.

specimens contain 10 tests at the longitudinal strains $\epsilon_1 = 0.02$, $\epsilon_2 = 0.04$, $\epsilon_3 = 0.08$, $\epsilon_4 = 0.12$, $\epsilon_5 = 0.16$, $\epsilon_6 = 0.18$, $\epsilon_7 = 0.20$, $\epsilon_8 = 0.24$, $\epsilon_9 = 0.28$, and $\epsilon_{10} = 0.32$. Each test was performed on a new sample. No necking of specimens was observed even at the highest longitudinal strain $\epsilon_{10}$. In the $m$th relaxation test ($m = 1, \ldots, 10$), a specimen was loaded with the cross-head speed 5 mm/min up to the longitudinal strain $\epsilon_m$ that was preserved constant during the relaxation time $t_r = 20$ min.

The engineering stress, $\sigma_e$, is plotted versus the logarithm of time $t$ in Figs. 5 and 6 for specimens annealed at $T = 110\,^{\circ}C$, in Figs. 7 and 8 for samples annealed at $T = 120\,^{\circ}C$, and in Figs. 9 and 10 for samples annealed at $T = 130\,^{\circ}C$. The experimental data show that the elongation ratio, $\lambda$, strongly affects the shape of relaxation curves. This is clearly shown in Figs. 5, 7 and 9, where the relaxation curves are depicted for strains in the sub-yield region.

Following common practice, the experimental data in Figs. 4–10 are plotted in the time interval between 10 and $10^3$ s. The initial response is excluded from the consideration, because the relaxation curves in the interval $0 \le t < 10$ s are noticeably affected by deformations during the loading period.

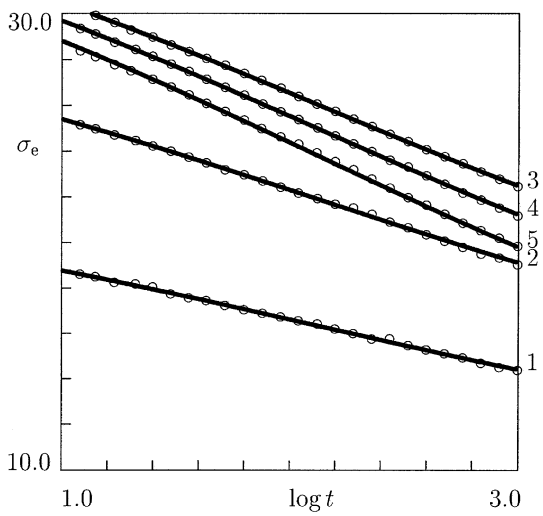


Fig. 7. The engineering stress $\sigma_e$ (MPa) versus time $t$ (s) in tensile relaxation tests on specimens annealed at $T = 120\,^{\circ}C$. Circles: experimental data. Solid lines: results of numerical simulation. Curve 1: $\epsilon = 0.02$; curve 2: $\epsilon = 0.04$; curve 3: $\epsilon = 0.08$; curve 4: $\epsilon = 0.12$; curve 5: $\epsilon = 0.16$.

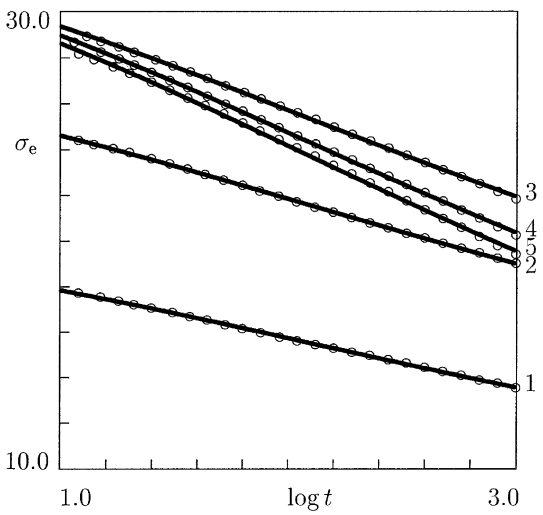


Fig. 9. The engineering stress $\sigma_e$ (MPa) versus time $t$ (s) in tensile relaxation tests on specimens annealed at $T = 130\,^{\circ}C$. Circles: experimental data. Solid lines: results of numerical simulation. Curve 1: $\epsilon = 0.02$; curve 2: $\epsilon = 0.04$; curve 3: $\epsilon = 0.08$; curve 4: $\epsilon = 0.12$; curve 5: $\epsilon = 0.16$.

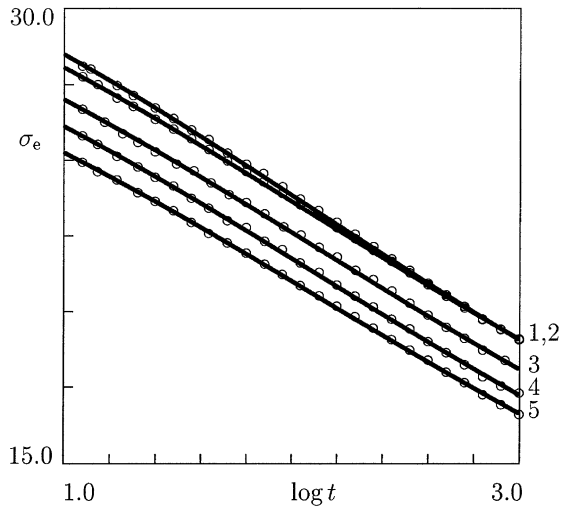


Fig. 10. The engineering stress $\sigma_e$ (MPa) versus time $t$ (s) in tensile relaxation tests on specimens annealed at $T = 130$ °C. Circles: experimental data. Solid lines: results of numerical simulation. Curve 1: $\epsilon = 0.18$; curve 2: $\epsilon = 0.20$; curve 3: $\epsilon = 0.24$; curve 4: $\epsilon = 0.28$; curve 5: $\epsilon = 0.32$.

## 7. Fitting of observations

Our purpose now is to find adjustable parameters in the constitutive Eq. (49) by matching the observations in relaxation tests. We do not dwell on the approximation of the stress–strain curves depicted in Figs. 2 and 3, because fitting of these curves with the help of Eqs. (43) and (44) requires the strain energy per strand, $w$, to be determined. With reference to Sweeney and Ward [33,34], we suppose that the mechanical energy, $w$, based on the slip-link model of rubber elasticity [44] may provide an adequate description of observations, but a detailed analysis of the experimental data will be reported elsewhere.

We begin with matching the relaxation curve for a specimen annealed at $T = 110$ °C and strained up to $\epsilon_2 = 0.04$. This strain is chosen because it is located substantially below the yield point, on the one hand, and the testing device ensures high accuracy of control of the strain level in the relaxation mode, on the other. Introducing the notation

$$C_0(\lambda) = \sigma_0(\lambda), \qquad C_1(\lambda) = -\kappa_a(\lambda)\sigma_0(\lambda), \tag{50}$$

we present Eq. (49) as follows:

$$\sigma_e(t,\lambda) = C_0(\lambda) + p_0 C_1(\lambda) \int_0^\infty \times [1 - \exp(-\exp(-z)t)] \exp\left[-\frac{(z-\Omega)^2}{2\Sigma^2}\right] dz. \tag{51}$$

Eq. (51) is determined by four experimental constants: $\Omega$, $\Sigma$, $C_0$ and $C_1$. To find these quantities, we fix the intervals $[0, \Omega_{max}]$ and $[0, \Sigma_{max}]$, where the 'best-fit' parameters $\Omega$ and $\Sigma$ are assumed to be located, and divide these intervals into $M$ sub-intervals by the points $\Omega_i = i\Delta_\Omega$ and $\Sigma_j = j\Delta_\Sigma$ $(i,j = 1,\dots,M)$ with $\Delta_\Omega = \Omega_{max}/M$, $\Delta_\Sigma = \Sigma_{max}/M$. For any pair, $\{\Omega_i, \Sigma_j\}$, we evaluate the integral in Eq. (51) numerically (by Simpson's method with 200 points and the step $\Delta_z = 0.08$). The pre-factor $p_0$ is determined by Eq. (48). The coefficients $C_0 = C_0(i,j)$ and $C_1 = C_1(i,j)$ are found by the least-squares method from the condition of minimum of the function

$$\Psi(i,j) = \sum_{t_m} [\sigma_{exp}(t_m) - \sigma_{num}(t_m)]^2,$$

where the sum is calculated over all experimental points $t_m$, $\sigma_{exp}$ is the engineering stress measured in the relaxation test, and $\sigma_{num}$ is given by Eq. (51). The best-fit parameters $\Omega$ and $\Sigma$ minimize the function $\Psi$ on the set $\{\Omega_i, \Sigma_j\ (i,j = 1,\dots,M)\}$. After determining the best-fit values, $\Omega_i$ and $\Sigma_j$, we repeat this procedure for the new intervals $[\Omega_{i-1}, \Omega_{i+1}]$ and $[\Sigma_{j-1}, \Sigma_{j+1}]$ to ensure good accuracy of fitting. The best-fit parameters read $\Omega = 5.42$ and $\Sigma = 4.64$.

For the quasi-Gaussian distribution function (47), the quantities $\Omega$ and $\Sigma$ do not coincide with the average potential energy for detachment of active strainds, $\Omega_0$, and the standard deviation of potential energies for separation of strands from the network, $\Sigma_0$. The latter quantities read

$$\Omega_0 = \int_0^\infty \omega p(\omega)\, d\omega, \qquad \Sigma_0 = \left[\int_0^\infty (\omega - \Omega_0)^2 p(\omega)\, d\omega\right]^{1/2}.$$

Numerical integration implies that $\Omega_0 = 6.32$ and $\Sigma_0 = 3.63$. The width of the quasi-Gaussian distribution $\xi = \Sigma_0/\Omega_0$ equals 0.57, which confirms the correctness of transition from Eqs. (46) and (47) to the governing Eq. (49).

To approximate relaxation curves at other strains, $\epsilon_m$, for specimens annealed at $T = 110$ °C, as well as for samples annealed at other temperatures, $T$, and for specimens not subjected to thermal treatment, we fix the constants $\Omega$ and $\Sigma$ and fit every relaxation curve by using two adjustable parameters, $C_0$ and $C_1$, which are determined by the least-squares technique. Figs. 4–10 demonstrate excellent agreement between the experimental data and the results of numerical simulation.

For any elongation ratio, $\lambda$, the fraction of active MRs, $\kappa_a(\lambda)$, is found from Eq. (50)

$$\kappa_a(\lambda) = -\frac{C_1(\lambda)}{C_0(\lambda)}.$$

This quantity is plotted versus the first principal invariant, $J_1$, of the right Cauchy–Green tensor for transition from the initial state to the deformed state in Figs. 11–14. According to Eq. (42), the parameter $J_1$ is given by

$$J_1 = \lambda^2 + 2\lambda^{-1}.$$

The experimental data are approximated by the

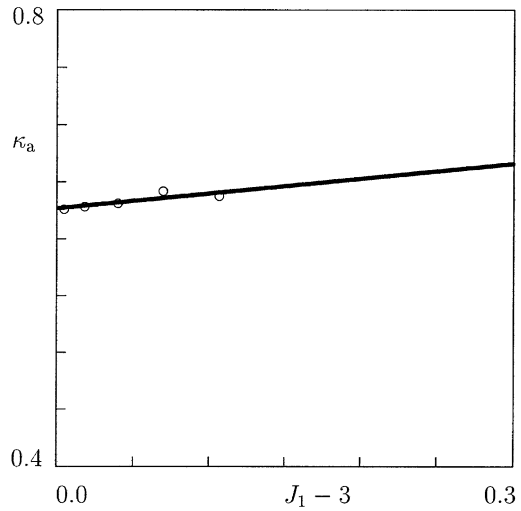


Fig. 11. The concentration of active MRs $\kappa_a$ versus the first principal invariant $J_1$ of the Cauchy–Green tensor for non-annealed specimens. Circles: treatment of observations. Solid lines: approximation of the experimental data by Eq. (52) with $\kappa_0 = 0.627$, $\kappa_1 = 0.130$.

phenomenological equation

$$\kappa_a = \kappa_0 + \kappa_1(J_1 - 3), \tag{52}$$

where the coefficients $\kappa_0$ and $\kappa_1$ are found by the least-squares method. According to the statistical theory of rubber elasticity, the quantity $J_1 - 3$ is proportional to the strain energy of a rubbery polymer. Eq. (52) implies that the content of active meso-regions linearly increases with the mechanical energy of amorphous regions modeled as networks of flexible chains.

Fig. 11 shows that Eq. (52) correctly describes the experimental data for non-annealed specimens. Figs. 12–14 reveal that the observations for annealed samples obey Eq. (52) with different coefficients $\kappa_0$ and $\kappa_1$ in the sub-critical and post-critical regions. These coefficients, as well as the strain, $\epsilon_{cr}$, corresponding to transition from the sub-critical region (small elongations) to the post-critical region (large elongations) are listed in Table 1.

Our aim now is to compare the changes in the coefficients $\kappa_0$ and $\kappa_1$ driven by an increase in the annealing temperature

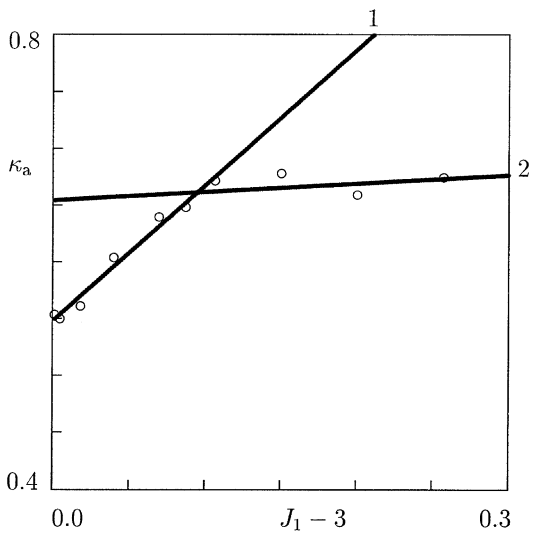


Fig. 12. The concentration of active MRs $\kappa_a$ versus the first principal invariant $J_1$ of the Cauchy–Green tensor for specimens annealed at $T = 110$ °C. Circles: treatment of observations. Solid lines: approximation of the experimental data by Eq. (52). Curve 1: $\kappa_0 = 0.548$, $\kappa_1 = 1.191$; curve 2: $\kappa_0 = 0.654$, $\kappa_1 = 0.074$.

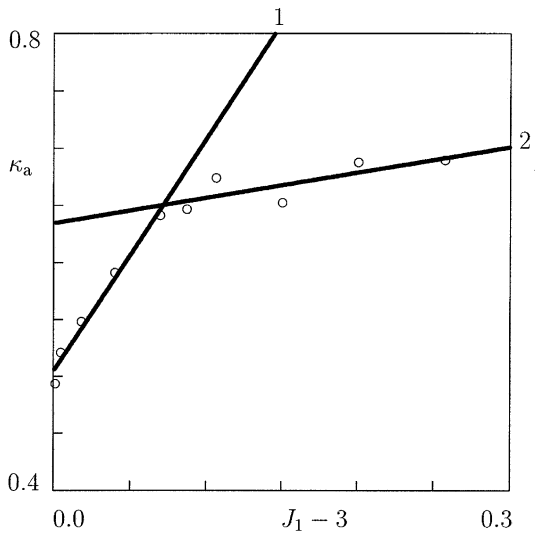


Fig. 13. The concentration of active MRs $\kappa_a$ versus the first principle invariant $J_1$ of the Cauchy–Green tensor for specimens annealed at $T = 120$ °C. Circles: treatment of observations. Solid lines: approximation of the experimental data by Eq. (52). Curve 1: $\kappa_0 = 0.505$, $\kappa_1 = 2.029$; curve 2: $\kappa_0 = 0.635$, $\kappa_1 = 0.221$.

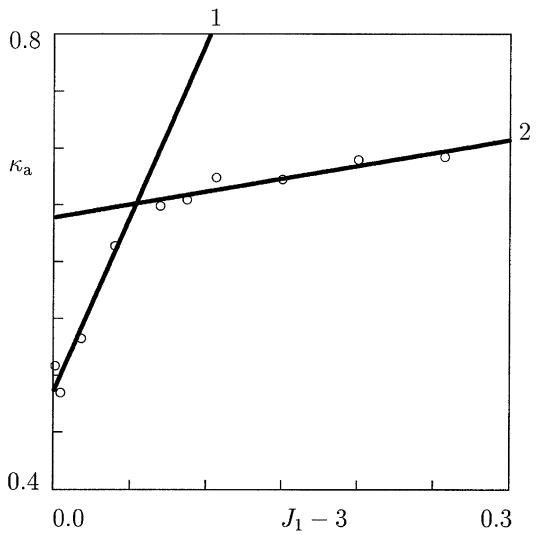


Fig. 14. The concentration of active MRs $\kappa_a$ versus the first principle invariant $J_1$ of the Cauchy–Green tensor for specimens annealed at $T = 130$ °C. Circles: treatment of observations. Solid lines: approximation of the experimental data by Eq. (52). Curve 1: $\kappa_0 = 0.486$, $\kappa_1 = 3.059$; curve 2: $\kappa_0 = 0.639$, $\kappa_1 = 0.227$.

Table 1
Adjustable parameters $\epsilon_{cr}$, $\kappa_0$ and $\kappa_1$ for iPP annealed at various temperatures $T$ °C

| $T$ | $\epsilon_{cr}$ | Sub-critical region | | Post-critical region | |
|---|---|---|---|---|---|
| | | $\kappa_0$ | $\kappa_1$ | $\kappa_0$ | $\kappa_1$ |
| 110 | 0.20 | 0.55 | 1.19 | 0.65 | 0.07 |
| 120 | 0.16 | 0.50 | 2.03 | 0.64 | 0.22 |
| 130 | 0.14 | 0.49 | 3.06 | 0.64 | 0.23 |

$T$ with the changes in the shape of melting curves presented in Fig. 1.

## 8. Discussion

Fig. 1 demonstrates that annealing of iPP results in the development of the second broad endotherm on the low-temperature side of the main peak of melting curves. Despite substantial interest to the kinetics of growth of the low-temperature shoulder on DSC traces of semicrystalline polymers [3,4,7,8,11], this phenomenon remains the subject of debate.

Several mechanisms have been proposed for the secondary crystallization of isotactic polypropylene at annealing:

1. Broadening of the distribution of crystalline lamellae with various strengths (stabilities) [7].
2. Melting–recrystallization of subsidiary (thin) lamellae.
3. The presence of two populations of lamellae with different growth rates (whose melting is attributed to low and high peaks on melting curves) [1].
4. Transformation of folded chain crystals into extended chain crystals [2].
5. Formation of β crystallites at annealing in the temperature range between 110 and 130 °C [11].

With reference to Verma et al. [1] and Hikosaka et al. [2], we focus on the following changes in the morphology of semicrystalline polymers driven by annealing at an elevated temperature:

1. Secondary crystallization of part of the amorphous phase in liquid pockets between stacks of primary lamellae and formation of individual subsidiary (thin) lamellae and their stacks.
2. Growth of primary (thick) lamellae with tapered shapes, which is governed by two mechanisms: (i) lateral growth by merging new folded chains to a crystal at its periphery, and (ii) 'thickening growth' by transformation of folded chains into extended chains in the central zone of a lamella.

At relatively low temperatures, in the interval between 100 and 150 °C, melting of primary lamellae may be disregarded. This implies that the DSC traces depicted in Fig. 1 are not affected (or, at least, are weakly affected) by thickening of primary lamellae. The differences between the melting curves for samples not subjected to thermal treatment and for specimens annealed at different temperatures are attributed to the development of subsidiary lamellae.

Formation of thin lamellae between stacks of primary lamellae is characterized by the nucleation rate and the rate of lateral growth. As a first approximation, we suppose that far below the melting point the nucleation and growth processes for subsidiary lamellae are thermally activated, which implies that at the highest temperature of annealing, $T = 130$ °C, the number of secondary lamellae and their average size are substantially larger than those at the lowest temperature, $T = 110$ °C. As the intensity of melting for subsidiary lamellae is inversely proportional to their length, secondary lamellae crystallized at $T = 110$ °C start to melt earlier than those crystallized at $T = 130$ °C. This is confirmed by DSC traces plotted in Fig. 1, which demonstrate that the low-temperature endotherm for specimens annealed at 110 °C exceeds that for specimens annealed at $T = 130$ °C in the interval of temperatures between 110 and 135 °C. With the growth of temperature in a DSC scan, the number of unmelted subsidiary lamellae developed at 110 °C dramatically decreases, which implies that the melting curve for specimens annealed at this temperature approaches the melting curve for specimens not subjected to thermal treatment when temperature reaches 140 °C. On the contrary, the low-temperature shoulder on the melting curve for samples annealed at 130 °C remains noticeably higher than that for non-annealed specimens.

The observed changes in melting curves of samples annealed at various temperatures, $T$, are compared now with changes in the $\kappa_a(\lambda)$-curves in the sub-critical region reported in Figs. 11–14. Formation of secondary lamellae and their stacks imposes extra restrictions on rearrangement of chains in amorphous meso-regions, which implies that the concentration of active meso-domains in a stress-free polymer should decrease at annealing. This conclusion is confirmed by Table 1. The decrease in $\kappa_a$ in stress-free specimens is estimated as 11% (from 0.55 at $T = 110$ °C to 0.49 at $T = 130$ °C), which appears to be comparable with changes in the DSC traces presented in Fig. 1. Under stretching in the sub-critical region, thin lamellae are broken one after another releasing the amorphous phase located in between stacks of primary (thick) lamellae. In Figs. 11–14 this release is observed as a monotonic increase in the concentration of active meso-regions with elongation ratio. In accord with Aboulfaraj et al. [27] and Coulon et al. [25], an individual thin lamella or a stack of subsidiary lamellae may be thought of as a deformable ribbon (see Figure 15 in Ref. [25]). Stretching a specimen causes elongation, bending and twisting of this ribbon, which, finally, induce its fracture. The ratio, $l$, of the average length of a ribbon to

the characteristic size of its cross-section may be employed for a rough estimate of the mechanically driven fracture of secondary lamellae. The higher the dimensionless ratio $l$ is, the lower strain is necessary for breakage of thin lamellae. As (i) the rate of lateral growth of subsidiary lamellae noticeably exceeds the rate of their thickening growth, and (ii) both these rates increase with temperature, it is natural to expect that thin lamellae developed at the highest temperature of annealing, $T = 130$ °C, have the largest value of $l$ and break at smaller elongations of a specimen than those formed at the lowest temperature, $T = 110$ °C. This hypothesis is fairly well confirmed by the data plotted in Figs. 11–14. Table 1 reveals that the rate of fragmentation of secondary lamellae under straining (which is characterized by the parameter $\kappa_1$, the rate of release of amorphous phase with the growth of elongation ratio) for samples annealed at 130 °C exceeds that for specimens annealed at 110 °C by a factor of 3.

The upper boundary of the sub-critical region is attributed to the strain, at which all thin lamellar stacks are broken. This point is observed in Figs. 11–14 as a point where the slope of the straight line (Eq. (52)) noticeably decreases. According to Table 1, the critical strain, $\epsilon_{cr}$, strongly decreases with annealing temperature $T$ (because lamellae with larger ratio $l$ are broken at smaller elongations). For the specimens under investigation, the critical strain is located in the interval between 0.14 and 0.20, i.e. between the apparent yield points defined as (i) the points of maxima on the engineering stress–engineering strain diagram (Fig. 2) and (ii) the points of transition to a developed plastic flow (Fig. 3). Whether the critical strain, $\epsilon_{cr}$, may be identified as the 'true' yield point remains an open question. To provide some answer to this question, relaxation of stresses should be analyzed on specimens annealed at higher temperatures (from $T = 140$ to $T = 160$ °C), where annealing noticeably affects the viscoplastic response of isotactic polypropylene. These results will be reported in a subsequent study.

The concentration of active meso-regions at the critical strain, $\epsilon_{cr}$, is practically independent of the annealing temperature (it equals 0.62 for samples not subjected to thermal treatment and varies from 0.64 to 0.65 for annealed specimens). This indicates that the growth of primary lamellae at annealing does not impose extra constrains on rearrangement of chains in the amorphous phase. A very weak increase in $\kappa_a$ for annealed specimens compared to its value for non-annealed samples may be attributed to melting of tangential lamellae in iPP and their recrystallization into radial lamellae at annealing.

According to Table 1, the rate of breakage of primary lamellae at straining of specimens in the post-critical region (which is characterized by the coefficient $\kappa_1$) noticeably grows with annealing temperature (it increases from 0.07 at $T = 110$ °C to 0.23 at $T = 130$ °C). This growth is ascribed by an increase in the dimensionless ratio $l$ at annealing at elevated temperatures, as well as by uncoiling of chains (transformation of folded chains into extended chains) in the central zones of lamellae. The latter implies a substantial reduction in the bending and twisting rigidity of lamellae, which enhances their breakage.

Fig. 3 demonstrates that necking of annealed specimens occurs at the elongation ratio $\lambda \approx 1.34$. It follows from Eq. (52) and Table 1 that the concentration of active meso-regions at the necking point insignificantly varies (from 0.68 to 0.70) for specimens annealed at different temperatures. Necking of specimens not subjected to thermal treatment occurs when the content of active meso-domains equals 0.64. This difference is quite comparable with the difference between the concentrations of active meso-domains at the critical strain (0.62 versus 0.64–0.65) and may be attributed to melting–recrystallization of tangential lamellae at annealing. On the basis of these observations, a hypothesis is suggested that necking of iPP specimens at stretching occurs when 'weak' lamellae (both primary and secondary) are broken. Further fragmentation of 'strong' lamellae by the coarse slip mechanism becomes energetically unfavorable (because it results in a negligible release of rigid amorphous fraction), which implies that the minimum of free energy is reached when a specimen becomes subjected to spatially inhomogeneous deformation in the necking region.

## 9. Concluding remarks

A model has been developed for the viscoelastic and viscoplastic responses of semicrystalline polymers at isothermal loading with finite strains. To derive constitutive equations, a complicated microstructure of a polymer is replaced by an equivalent transient network of macromolecules bridged by junctions (physical cross-links, entanglements and crystalline lamellae). The network is thought of as an ensemble of meso-regions with various potential energies for separation of strands from temporary nodes.

The viscoelastic response of a semicrystalline polymer is attributed to (i) separation of active strands from temporary junctions in active meso-domains and (ii) merging of dangling strands with the network. Rearrangement of strands is treated as a thermally activated process, whose rate is determined by the Eyring equation.

The viscoplastic behavior is ascribed to sliding of junctions with respect to their positions in the bulk material. Stress–strain relations and a kinetic equation for the rate of sliding have been developed by using the laws of thermodynamics. Unlike conventional models in viscoplasticity, it is demonstrated that in the general case the rate-of-strain tensor for plastic flow is not proportional to the deviatoric component of the Cauchy stress tensor. These tensors remain proportional for deformations without

rotations, when the left and right Cauchy–Green tensors coincide.

Governing equations are simplified for uniaxial tension of a bar. Adjustable parameters are found by fitting experimental data in relaxation tests at strains below the necking point.

Four series of tensile relaxation tests have been performed on isotactic polypropylene at ambient temperature. In the first series, injection-molded samples were used without thermal pre-treatment. In the other series, the samples were annealed for 24 h at 110, 120 and 130 °C, respectively, and slowly cooled by air. The results of mechanical experiments were compared with DSC melting curves.

The following conclusions have been drawn:

1. Fair agreement is demonstrated between the experimental data in relaxation tests and the results of numerical simulation under the assumption that the relaxation spectrum of iPP (which is characterized by the distribution function, $p(\omega)$, for potential energies of detachment of active strands from temporary junctions) is not affected by thermo-mechanical factors.
2. The relaxation strength (which is characterized by the content of active meso-regions $\kappa_a$) increases with strain. Changes in the concentration of active meso-domains are attributed to mechanically induced fragmentation of lamellae. An increase in $\kappa_a$ at stretching is proportional to the first principal invariant of the Cauchy–Green tensor.
3. Two regions of strains are revealed by matching relaxation curves. In the sub-critical region, the rate of growth in $\kappa_a$ is relatively large. An increase in the content of active amorphous domains is ascribed to fragmentation of subsidiary (thin) lamellae developed at annealing. This is confirmed by changes in the DSC traces observed in calorimetric tests. In the post-critical region, the concentration of active MRs increases rather weakly. This growth reflects release of constrained amorphous phase driven by breakage of primary (thick) lamellae.
4. The critical strain, $\epsilon_{cr}$, that separates these two regions, decreases with annealing temperature. This is explained by an increase in brittleness of secondary lamellae developed at higher temperatures (the rate of their lateral growth substantially exceeds the rate of thickening growth, which implies that their bending and twisting rigidities are reduced with an increase in the annealing temperature).
5. For specimens annealed at various temperatures, the critical strain is rather close to the yield strain, which means that yielding of iPP may be attributed to transition from breakage of secondary lamellae to fragmentation of primary lamellae.
6. At the necking point, the concentration of active meso-regions reaches approximately the same value for all samples. This means that necking (transition from homogeneous to heterogeneous deformation of a specimen) may be associated with the elongation level, at which further destruction of crystallites becomes energetically unfavorable, because it results in a negligibly small release of the constrained amorphous phase.

## References


[1] Verma R, Marand H, Hsiao B. Macromolecules 1996;29:7767–75.
[2] Hikosaka M, Amano K, Rastogi S, Keller A. Macromolecules 1997; 30:2067–74.
[3] Al-Raheil IA, Qudah AM, Al-Share M. J Appl Polym Sci 1998;67: 1267–71.
[4] Alamo RG, Brown GM, Mandelkern L, Lehtinen A, Paukkerri R. Polymer 1999;40:3933–44.
[5] Alizadeh A, Richardson L, Xu J, McCartney S, Marand H, Cheung YW, Chum S. Macromolecules 1999;32:6221–35.
[6] Marand H, Alizadeh A, Farmer R, Desai R, Velikov V. Macromolecules 2000;33:3392–403.
[7] Iijima M, Strobl G. Macromolecules 2000;33:5204–14.
[8] Maiti P, Hikosaka M, Yamada K, Toda A, Gu F. Macromolecules 2000;33:9069–75.
[9] Weglarz WP, Peemoeller H, Rudin A. J Polym Sci, B: Polym Phys 2000;38:2487–506.
[10] Alizadeh A, Sohn S, Quinn J, Marand H, Shank LC, Iler HD. Macromolecules 2001;34:4066–78.
[11] Labour T, Gauthier C, Seguela R, Vigier G, Bomal Y, Orange G. Polymer 2001;42:7127–35.
[12] Ward IM, Wolfe JM. J Mech Phys Solids 1966;14:131–40.
[13] Ward IM, Hadley DW. An introduction to the mechanical properties of solid polymers. New York: Wiley; 1993.
[14] Smart J, Williams JG. J Mech Phys Solids 1972;20:313–24.
[15] Wortmann F-J, Schulz KV. Polymer 1994;35:2108–19.
[16] Wortmann F-J, Schulz KV. Polymer 1995;36:2363–9.
[17] Ariyama T. J Mater Sci 1996;31:4127–31.
[18] Ariyama T, Mori Y, Kaneko K. Polym Engng Sci 1997;37:81–90.
[19] Dutta NK, Edward GH. J Appl Polym Sci 1997;66:1101–15.
[20] Read BE, Tomlins PE. Polymer 1997;38:4617–28.
[21] Tomlins PE, Read BE. Polymer 1998;39:355–67.
[22] Andreassen E. Polymer 1999;40:3909–18.
[23] Seguela R, Staniek E, Escaig B, Fillon B. J Appl Polym Sci 1999;71: 1873–85.
[24] Kalay G, Bevis MJ. J Polym Sci, B: Polym Phys 1997;35:241–63. see also p. 265–91.
[25] Coulon G, Castelein G, G'Sell C. Polymer 1998;40:95–110.
[26] Labour T, Ferry L, Gauthier C, Hajji P, Vigier G. J Appl Polym Sci 1999;74:195–200.
[27] Aboulfaraj M, G'Sell C, Ulrich B, Dahoun A. Polymer 1995;36: 731–42.
[28] Nitta K-H, Takayanagi M. J Polym Sci, B: Polym Phys 1999;37: 357–68.
[29] Nitta K-H, Takayanagi M. J Polym Sci, B: Polym Phys 2000;38: 1037–44.
[30] Zhang XC, Butler MF, Cameron RE. Polym Int 1999;48:1173–8.
[31] Bergstrom JS, Kurtz SM, Rimnac CM, Edidin AA. Biomaterials 2002; 23:2329–43.
[32] Meyer RW, Pruitt LA. Polymer 2001;42:5293–306.
[33] Sweeney J, Ward IM. J Rheol 1995;39:861–72.
[34] Sweeney J, Ward IM. J Mech Phys Solids 1996;44:1033–49.
[35] Boyce MC, Socrate S, Llana PG. Polymer 2000;41:2183–201.
[36] Green MS, Tobolsky AV. J Chem Phys 1946;14:80–92.

[37] Yamamoto M. J Phys Soc Jpn 1956;11:413–21.
[38] Tanaka F, Edwards SF. Macromolecules 1992;25:1516–23.
[39] Krausz AS, Eyring H. Deformation kinetics. New York: Wiley; 1975.
[40] Kloczkowski A. Polymer 2002;43:1503–25.
[41] Derrida B. Phys Rev Lett 1980;45:79–82.
[42] Collar EP, Cofrades AG, Laguna O, Areso S, Garcia-Martinez JM. Eur Polym J 2000;36:2265–74.
[43] Wunderlich B. Crystal melting. Macromolecular physics, vol. 3. New York: Academic Press; 1980.
[44] Ball RC, Doi M, Edwards SF, Warner M. Polymer 1981;22:1010–8.